Article

Boosting Supercapacitor Energy Storage Using Microporous Carbon Derived from an Octavinylsilsesquioxane and Fluorenone-Linked Porous Hybrid Polymer

Abdul Basit, Mohamed Gamal Mohamed,* Mohsin Ejaz, Bo Xuan Su, Hina Manzoor,
and Shiao-Wei Kuo*

Cite This: ACS Appl. Energy Mater. 2024, 7, 7505–7516

Read Online

ACCESS | Metrics & More | Article Recommendations | Supporting Information

ABSTRACT: Supercapacitors (SCs), with their exceptional properties, offer a promising solution to the ongoing energy crisis, addressing the growing demand for high-energy storage devices. Polymeric organic porous materials (POIPs) exhibit various sizes, precisely controlled porosities, lightweight nature, extensive surface areas, impressive intrinsic porosity, attractive surface chemistry, outstanding stability, and customizable structures and functionalities. These features collectively render POIPs as a cost-effective material for applications in energy storage. This study successfully synthesized an octavinylsilsesquioxane (OVS)-FO-POIP through a Heck coupling reaction between OVS and 2,7-dibromo-9H-fluoren-9-one (DBFO). Confirmation of the OVS-FO-POIP's chemical structure was achieved using solid-state ^{13}C and ^{29}Si NMR and Fourier transform infrared analyses. Subsequently, carbonization and KOH activation at 900 °C yielded a porous carbon material, denoted as OVS-FO-POIP-900. Microporous characteristics were evidenced by specific surface area (S_{BET}) values of 264 m^2 g^{-1} for the OVS-FO-POIP and 387 m^2 g^{-1} for OVS-FO-POIP-900 and their corresponding pore diameters of 1.90 and 1.59 nm, respectively. Notably, OVS-FO-POIP-900 demonstrated an improved particular specific capacitance of 776 F g^{-1} compared to that of the OVS-FO-POIP (271 F g^{-1}) at a current density of 1 A g^{-1}, in addition to an exceptional capacitance retention of up to 79% after 6000 cycles. The heightened surface area enhances the probability of electrochemical reactions, thereby elevating capacitance levels. To delve deeper into electrochemical performance, symmetric devices were constructed for both the OVS-FO-POIP and the OVS-FO-POIP-900, exhibiting specific capacitances of 167 and 268 F g^{-1}, respectively. Remarkably, OVS-FO-POIP-900 demonstrated outstanding performance in these electrochemical assessments, suggesting its potential suitability for SC applications.
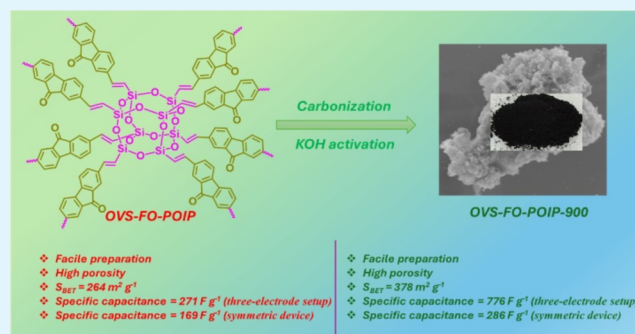
KEYWORDS: octavinylsilsesquioxane, fluorenone, hybrid porous polymer, porous carbon, thermal stability, supercapacitors

INTRODUCTION

Energy stands as the cornerstone for the sustenance and progression of a human society. Presently, there is a notably limited supply of traditional fossil fuels, possibly attributed to various factors including the rapid growth in both economic activity and society, alongside the escalating levels of contamination of the environment.[1−6] Despite numerous alternative methods accessible to address various requirements, such as renewable energy like solar, wind, and geothermal energy, solely relying on them may not be prudent. These sources not only aim to generate electricity but also face challenges related to their raw material supply.[7,8] Hence, given these ramifications and the pressing need to tackle the present scenario, it is vital to advance materials capable of efficiently managing the energy storage process.[8] Supercapacitors (SCs) or ultracapacitors, with their ability to provide high power and energy densities, occupy a middle ground between batteries and dielectric capacitors, effectively meeting all the mentioned requirements for high-energy storage systems.[9] Due to their remarkable attributes, SCs find uses including airbag deployment in cars, pacemakers, power backup systems, and electric vehicles.[10−13]

In general, SCs may be divided into three classes based on their structure, composition, and mode of operation: asymmetric capacitors (ACs), electric double-layer capacitors (EDLCs), and hybrid ion capacitors (HICs). These capacitors offer distinct benefits including sustained performance over
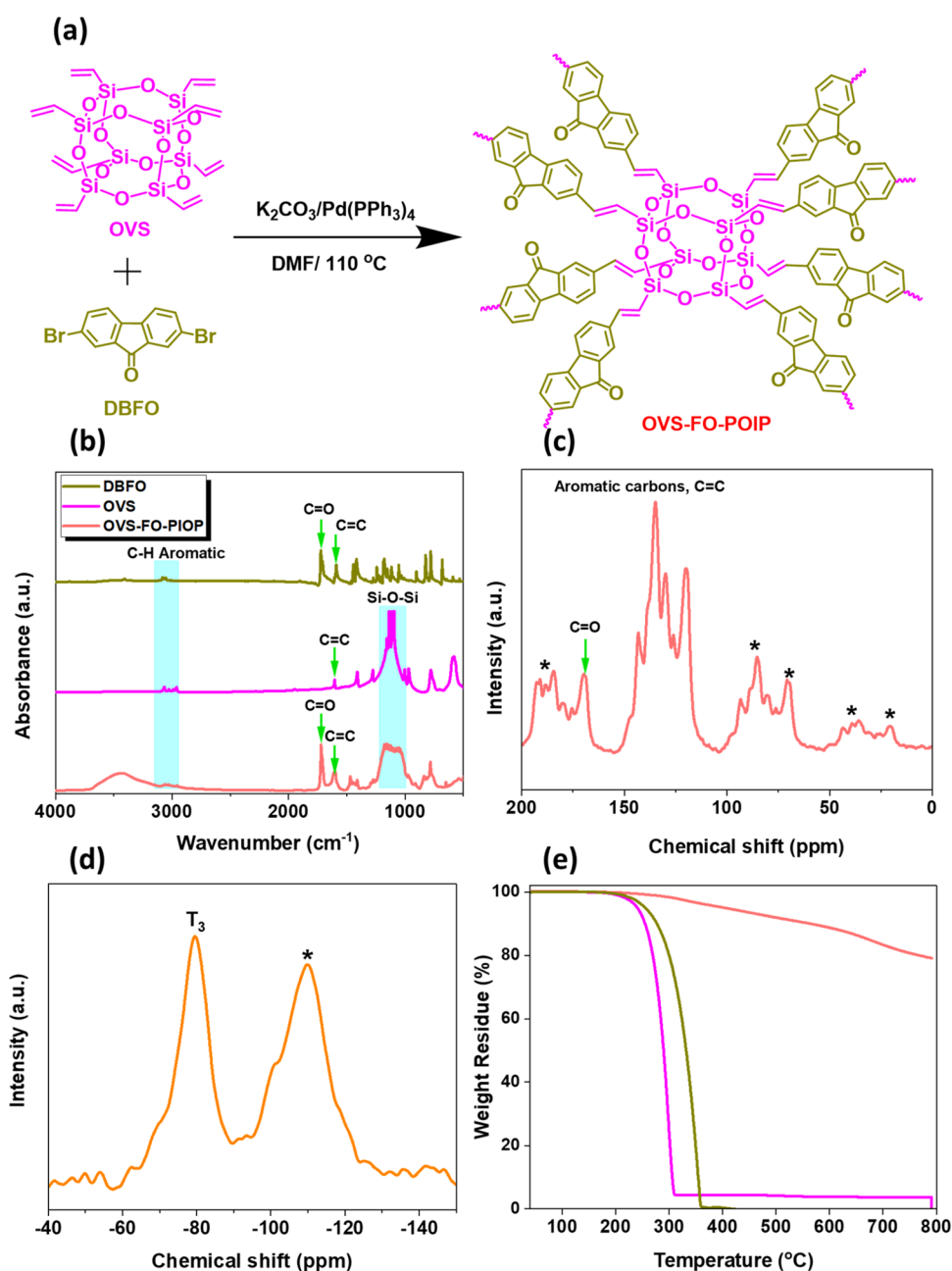
Figure 1. (a) Synthesis of OVS-FO-POIP through the Heck reaction, (b) Fourier transform infrared (FTIR) spectra of OVS, DBFO, and OVS-FO-POIP, (c) solid-state ^{13}C NMR of OVS-FO-POIP, (d) solid-state ^{29}Si NMR of OVS-FO-POIP, and (e) TGA of OVS, DBFO, and OVS-FO-POIP.

extended periods at high current densities. Specifically, they demonstrate an exceptional number of charging and discharging cycles, often regarded as infinite cycles. Moreover, they exhibit high Coulombic efficiency, as referenced in prior studies.[14−17] SCs differ from conventional capacitors in their utilization of ion-conducting electrolytes instead of dielectrics.[18] The remarkable attributes of SCs position them as exceptional possibilities for preserving energy devices.[19,20] Furthermore, these gadgets are crafted to establish an electrically charged dual layer at the junction of a solid porous electrode and a liquid electrolyte, to store energy.[21] Their rapid charging capability, extended temperature range, enhanced safety, environmental friendliness, and maintenance-free operation are distinguishing features. However, their lower energy densities compared to batteries restrict their applica-tions. Incorporating redox-active groups into carbonaceous materials can boost their performance, enabling them to combine the mechanisms of pseudocapacitors[22] and EDLC.[23−25]

Porous organic polymers (POPs) and porous organic−inorganic polymers (POIPs) are materials with multiple dimensions, characterized by precisely defined porosities, lightweight nature, high surface areas, exceptional inherent porosity, appealing surface chemical functionalities, outstanding stability, and structures and functions that are predesignable and adjustable.[26−29] Connected via strong covalent connections between different building units with different topologies, POPs and POIPS have garnered significant research interest as a result of their extensive uses for energy storage/conversion, heterogeneous catalysis, photoelectric
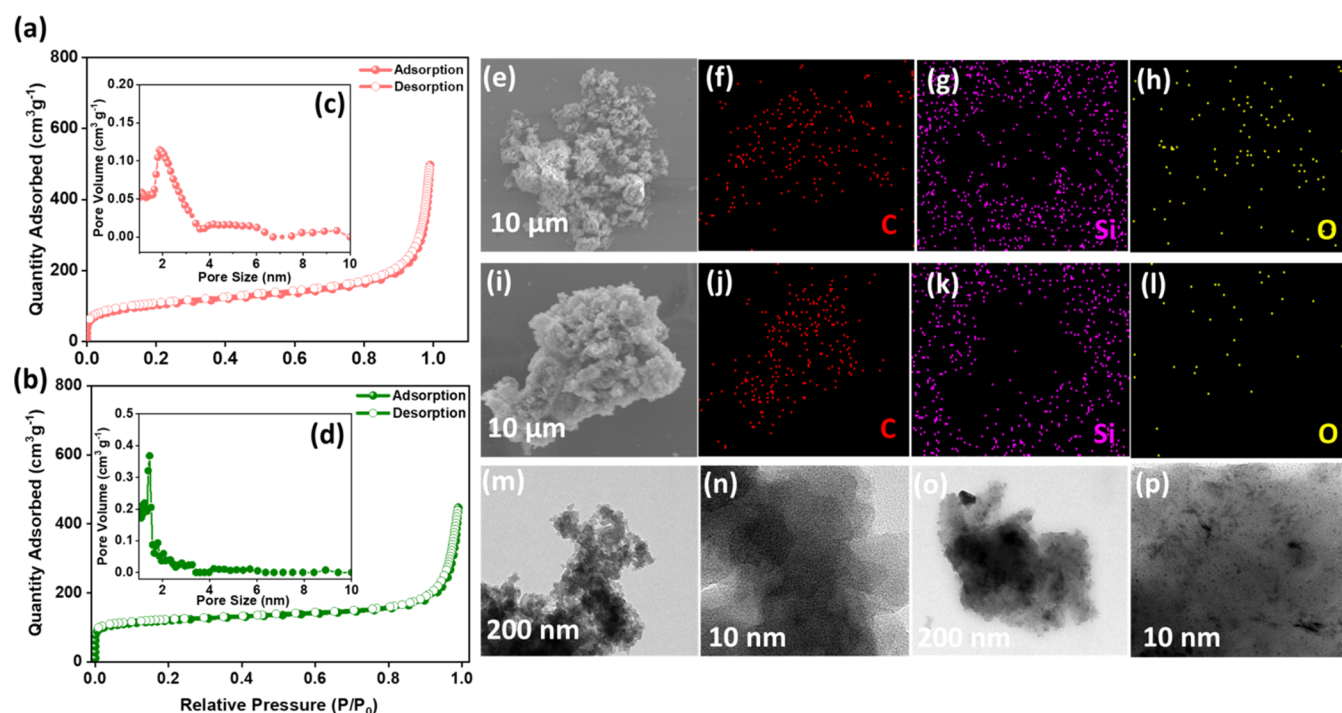
Figure 2. (a, b) N$_2$ adsorption−desorption isotherm, (c, d) pore size curves, (e, i) SEM images, (f−h, j−l) SEM-EDS mapping images, and (m−p) TEM images of OVS-FO-POIP (a, c, e, f, g, h, m, n) and OVS-FO-POIP-900 (b, d, i, j, k, l, o, p).

conversion, chemical and biosensing, absorption, optoelectronics, water treatment, and biomedical engineering.[30−45] Among hybrid nanoparticles, POSS, characterized by its distinctive three-dimensional structure and customizable physicochemical attributes, presents a unique opportunity for enhancing polymer composites. It could be integrated into these materials through either physical blending or chemical bonding methods, facilitating the acquisition of superior performance characteristics.[46−51] These particles exhibit a dual nature, blending material properties from both the inorganic siloxane cage and the organic groups situated at the periphery.[52] With their precisely defined nanostructure, they have garnered considerable interest in the field of hybrid materials science and engineering.[53] These units are particularly intriguing in the realm of energy storage due to their high surface area and impressive mechanical and thermal characteristics.[54] Incorporating POSS into porous polymers and porous hybrid polymers enhances their oxidation resistance as well as mechanical and thermal properties.[47,55−60] POSS also serves a crucial function in SC electrodes. Utilizing a block copolymer, hierarchically porous carbon structures are generated.[61,62] Evaluated within a symmetrical two-electrode cell employing a 1 M H$_2$SO$_4$ aqueous electrolyte at a rate of 0.25 A g^{-1}, these carbon materials demonstrate an exceptional specific surface area exceeding 2000 m^2 g^{-1} and a specific capacitance of 210 F g^{-1}.[63] According to Kuo et al.,[64] the research findings indicate that a microporous carbon framework (C-OVS-DDSQ) demonstrates a capacitance of 146 F g^{-1}. 9-Fluorenone (FO) is an aromatic organic compound with the chemical formula C$_{13}$H$_8$O. Its polarity arises from the oxygen atom within its five-membered ring.[65] The structure features a fluorene moiety with a ketone functional group at the 9-position. This compound is frequently used in the production of pigments and dyes. Additionally, it plays a

crucial role in the development of organic photovoltaics and organic light-emitting diodes (OLEDs).[65]

Using meticulous procedures, we synthesized an OVS-based POIP, named the OVS-FO-POIP, through a Heck coupling reaction involving the OVS and DBFO as building monomers, Figure 1a. Subsequently, we produced a porous carbon material (OVS-FO-POIP-900) by subjecting OVS-FO-POIP to carbonization and KOH activation at 900 °C. Both OVS-FO-POIP and OVS-FO-POIP-900 demonstrated microporous characteristics, showcasing significant surface areas and high capacitance. Our investigation thoroughly assessed the properties of these materials, covering porosity, morphology, and thermal degradation temperature (T_{d10}). Based on electrochemical results, the porous carbon material (OVS-FO-POIP-900) exhibited a specific capacitance value close to 776 F g^{-1} compared to 271 F g^{-1} for OVS-FO-POIP, with over 79% of the initial capacitance retained after 6000 cycles. In the corresponding symmetric SCs for OVS-FO-POIP-900, the sample demonstrated a specific capacitance of 268 F g^{-1}. This study marks a pivotal advancement and simple approach in leveraging the OVS moiety to prepare porous carbon (OVS-FO-POIP-900) as an electrode material for SCs.

■ EXPERIMENTAL SECTION

Materials. Potassium carbonate (K$_2$CO$_3$, 99.8%), octavinylsilsesquioxane (OVS), fluorenone (FO, 98%), bromine (Br$_2$) solution, methanol (MeOH), acetone, dimethylformamide (DMF), sodium sulfite (Na$_2$SO$_3$), and palladium tetrakis(triphenylphosphine) [Pd-(PPh$_3$)$_4$, 98%] were acquired from Sigma-Aldrich.

Synthesis of 2,7-Dibromo-9-fluorenone [DBFO]. FO (10.00 g, 55.40 mmol) was dissolved in 140 mL of H$_2$O and stirred for 30 min at 0 °C. Following this, Br$_2$ (8.5 mL, 165.2 mmol) was added. The reaction mixture was then allowed to stir for 10 h. After 10 h, 150 mL of extra H$_2$O and 150 mL of a Na$_2$SO$_3$ solution were added to the reaction mixture. Filtration and washing of the crude residue with
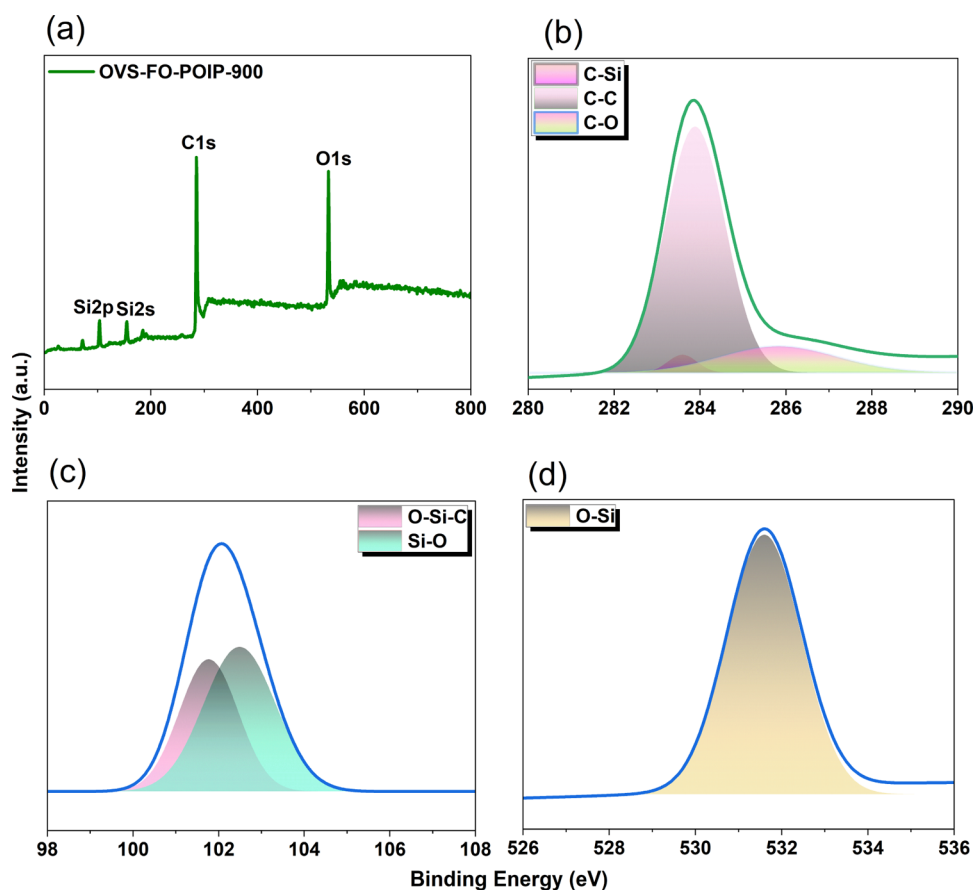
Figure 3. (a) XPS survey of OVS-FO-POIP-900 and (b−d) XPS fitting data for (b) carbon, (c) silicon, and (d) oxygen in the OVS-FO-POIP-900 framework.

water yielded DBFO as a yellow product (18.718 g). ^{1}H NMR (500 MHz, Figure S1): 7.80, 7.64, 7.40 ppm.

Synthesis of the OVS-FO-POIP. Under a nitrogen atmosphere, a mixture comprising 0.5 g of OVS, DBFO (1.02 g), K_2CO_3 (0.87 g), and $Pd(PPh_3)_4$ (0.04 g) was stirred in DMF under reflux conditions (110 °C) for 72 h. Subsequently, the orange powder of OVS-FO-POIP was isolated and subjected to washing with DMF, THF, and acetone.

Preparation of OVS-FO-POIP-900. Under N_2 gas, the OVS-FO-POIP sample was carbonized for 4 h at 600 °C at a heating rate of 5 °C min^{-1}, resulting in the production of a carbon black material. Subsequently, the carbonized sample underwent chemical activation with KOH in 1:1 ratio and was maintained at 900 °C for 3 h. Finally, OVS-FO-POIP-900 was obtained after washing the sample with a solution of HCl (2 N), water, and acetone, Figure S2.

RESULTS AND DISCUSSION

Synthesis and Characterization of the OVS-FO-POIP and OVS-FO-POIP-900. We synthesized OVS-FO-POIP through a Heck coupling reaction using OVS, DBFO, DMF, $Pd(PPh_3)_4$, and K_2CO_3 at 110 °C for 72 h, Figure 1a. The resulting material exhibited low solubility in organic solvents, indicating the successful development of a cross-linked porous material and a complete Heck reaction. Subsequently, the OVS-FO-POIP underwent carbonization at 600 °C for 4 h, followed by chemical activation with KOH (1:1) at 900 °C for 3 h, resulting in the production of OVS-FO-POIP-900, Figure S2. The chemical structure of OVS-FO-POIP was characterized using FTIR and NMR spectroscopy. The DBFO exhibited bands at 3076 and 1726 cm^{-1} for phenyl and C=O in the FO unit, respectively, Figure 1b. The FTIR spectrum of OVS-FO-POIP exhibited peaks at 3040, 1720, and 1108 cm^{-1}, which are equivalent to the CH aromatic, C=O, and Si−O−Si, respectively, Figure 1b. The successful formation of the OVS-FO-POIP can be attributed to the effective Heck reaction, as indicated by the broadening of the Si−O−Si peak and the presence of a distinct C=O absorption peak. Solid-state ^{13}C NMR analysis showed carbon nucleus signals in the range of 143−118 and 134−129 ppm, indicating the presence of C=C and aromatic carbons, respectively Figure 1c. Moreover, solid-state ^{29}Si NMR analysis confirmed the incorporation of OVS units into the OVS-FO-POIP framework, with a peak observed at −79.6 ppm, due to the T_3 group, Figure 1d. In thermogravimetric analysis (TGA), OVS-FO-POIP exhibited a percentage of carbon residue of 78 wt % and a T_{d10} at 533 °C. In contrast, as depicted in Figure 1e, OVS and DBFO decomposed at temperatures (T_{d10}) of 255 and 279 °C, respectively.

Using N_2 isotherms, we investigated the intricate pore characteristics of the OVS-FO-POIP and the OVS-FO-POIP-900. BET computation and the NLDFT model were employed to examine the specific surface area (S_{BET}), total pore volume (TPV), and average pore size (APS), respectively, Figure 2a−d. Figure 2a,b depicts the I-type isothermal curves of OVS-FO-POIP and OVS-FO-POIP-900. Notably, at pressures (P/P_0) below 0.01, the N_2 isotherm exhibits significant rises, indicating the presence of numerous micropores. For OVS-FO-POIP, S_{BET}, TPV, and APS values are 264 m^2 g^{-1}, 0.1 cm^3 g^{-1}, and 1.9 nm, respectively, Figure 2c, while for OVS-FO-POIP-900, these values are 387 m^2 g^{-1}, 0.4 cm^3 g^{-1}, and 1.51 nm,
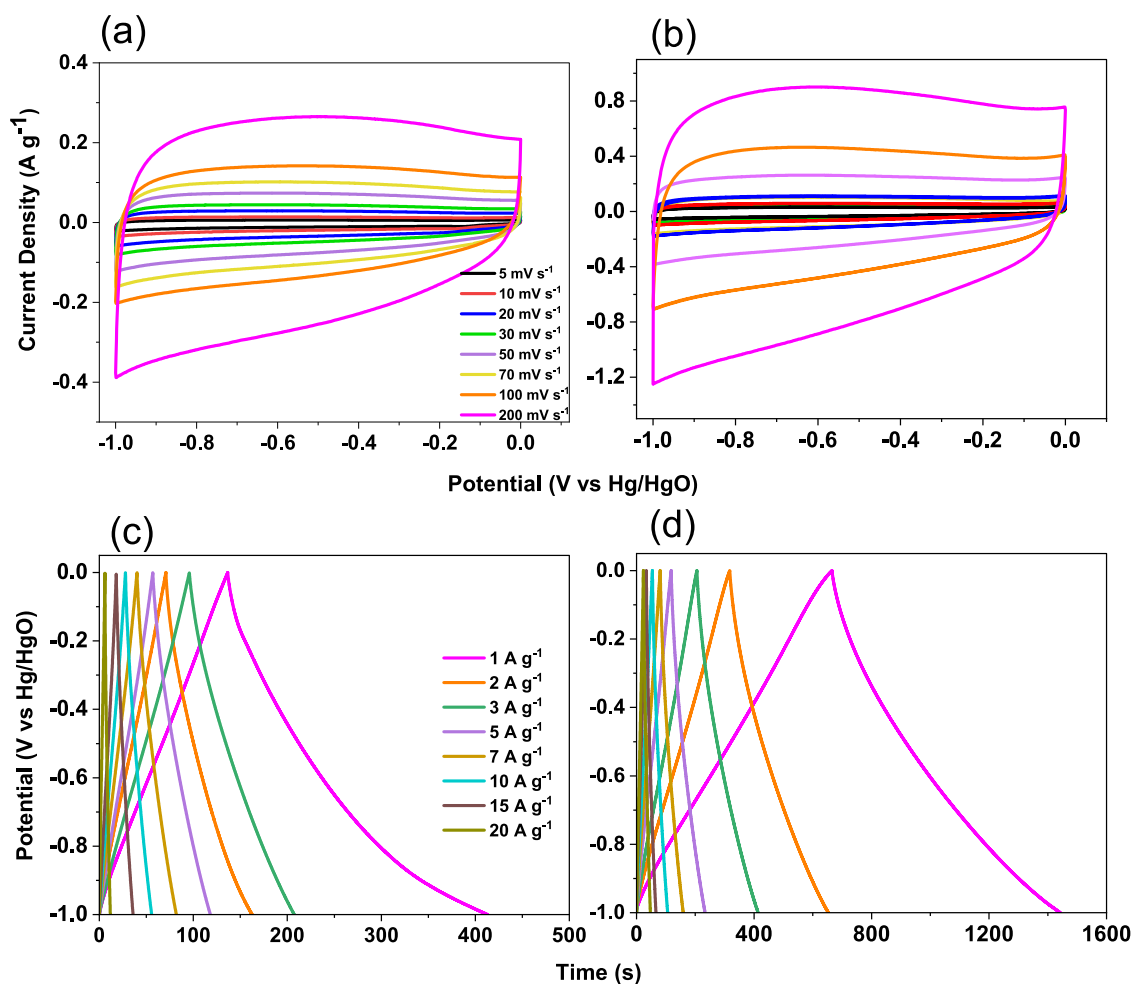
Figure 4. (a, b) CV and (c, d) GCD of (a, c) OVS-FO-POIP and (b, d) OVS-FO-POIP-900.

respectively, Figure 2d. Scanning electron microscopy (SEM)-energy dispersive X-ray spectroscopy (EDS) mapping, and transmission electron microscopy (TEM) were employed to examine the morphologies and elemental compositions [C, Si, and O] of the OVS-FO-POIP and the OVS-FO-POIP-900, Figure 2e–p. The SEM images revealed the presence of irregularly aggregated spherical structures in both OVS-FO-POIP and OVS-FO-POIP-900, Figure 2e,2i. SEM-EDS mapping, Figure 2f–l confirmed the presence of C (red), Si (violet), and O (yellow) within the frameworks of both materials. However, TEM images did not show a specific range order structure in either the OVS-FO-POIP or the OVS-FO-POIP-900, Figure 2m–p. Raman spectroscopy was utilized to analyze the defect structure of the OVS-FO-POIP-900, Figure S3. The peaks at 1322 and 1592 cm^{-1} represent the D band (disordered sp^3 carbon atoms) and G band (graphitic sp^2), respectively. The ratio of the intensity of the D band to the G band (I_D/I_G ratio) can be employed to assess the degree of graphitization in porous carbon structures. In OVS-FO-POIP-900, the presence of both graphitic and amorphous structures is indicated by an I_D/I_G value of 1.04, which could be beneficial for enhancing electrical conductivity.[66]

We utilized X-ray photoelectron spectroscopy (XPS) to confirm that Si, C, and O are present in the OVS-FO-POIP-900, Figure 3. XPS, a surface-sensitive analytical technique, provides insights into the elemental composition, surface chemistry, and electronic structure of materials. The signals corresponding to Si 2p, Si 2s, C 1s, and O 1s were observed at 103, 155, 284, and 532 eV, respectively, Figure 3a. Furthermore, fitted peaks for carbon, Figure 3b, were observed at 283.5, 283.8, and 285.9 eV, attributed to C–Si, C–C, and C–O, respectively. Additionally, fitted peaks for O–Si–C and O–Si were observed at 101.7 and 102.4 eV, respectively, Figure 3c, while oxygen displayed an O–Si peak at 531.6 eV, Figure 3d.

Electrochemical Performance of the OVS-FO-POIP and OVS-FO-POIP-900 Based on a Three-Electrode System. Using a three-electrode setup, we used galvanostatic charge–discharge (GCD) measurements and cyclic voltammetry (CV) to analyze the electrochemical characteristics. A 1 M KOH electrolyte was utilized with a Hg/HgO reference electrode and a platinum counter electrode. The CV curves, Figure 4a,b, spanning from −1 to 0 V at various scan rates (5–200 mV s^{-1}), displayed rectangular shapes devoid of discernible peaks, indicating predominant electric double-layer capacitance (EDLC) behavior. In cyclic voltammetry, the voltage applied to the EDLC is cyclically varied between the upper and lower limits, known as oxidation and reduction potentials. The current flowing through the EDLC during cycling provides crucial insights into its electrochemical behavior. Figure 4a,4b depicts the CV curves of OVS-FO-POIP and OVS-FO-POIP-900, respectively, confirming the electrical double-layer behavior. The high specific current is attributed to the high scan rate, maintaining the morphology of
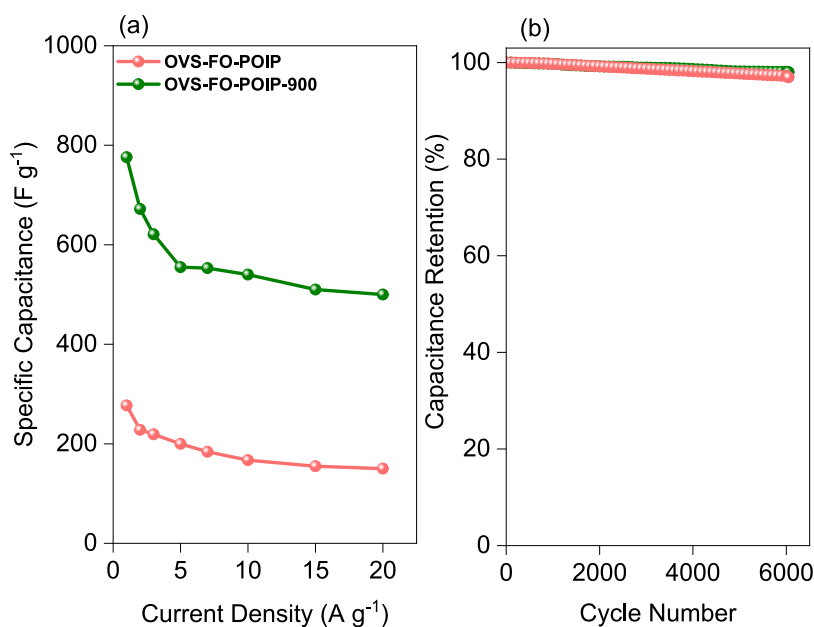
Figure 5. (a) Specific capacitance vs current density and (b) capacitance retention profile of OVS-FO-POIP and OVS-FO-POIP-900.
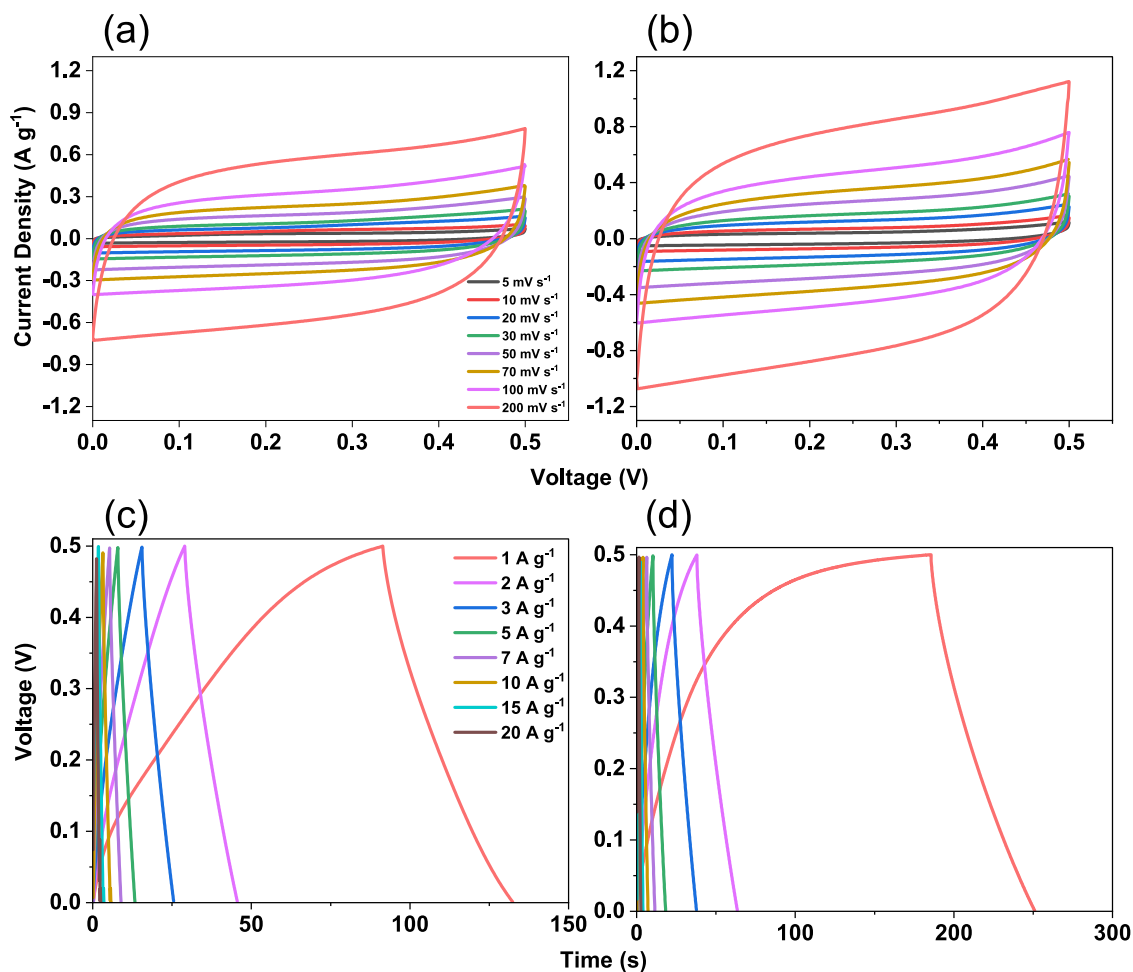
Figure 6. (a, b) CV and (c, d) GCD of symmetric coin cells of (a, c) OVS-FO-POIP and (b, d) OVS-FO-POIP-900.

the CV profiles. The specific capacitance values for OVS-FO-POIP and OVS-FO-POIP-900 were derived from their CV profiles, with the results summarized in Figure S4.

In a galvanostatic charge−discharge (GCD) test, Figure 4c,d, a constant current rate is applied to either charge (galvanostatic charge) or discharge (galvanostatic discharge) the supercapacitor while monitoring the voltage across the
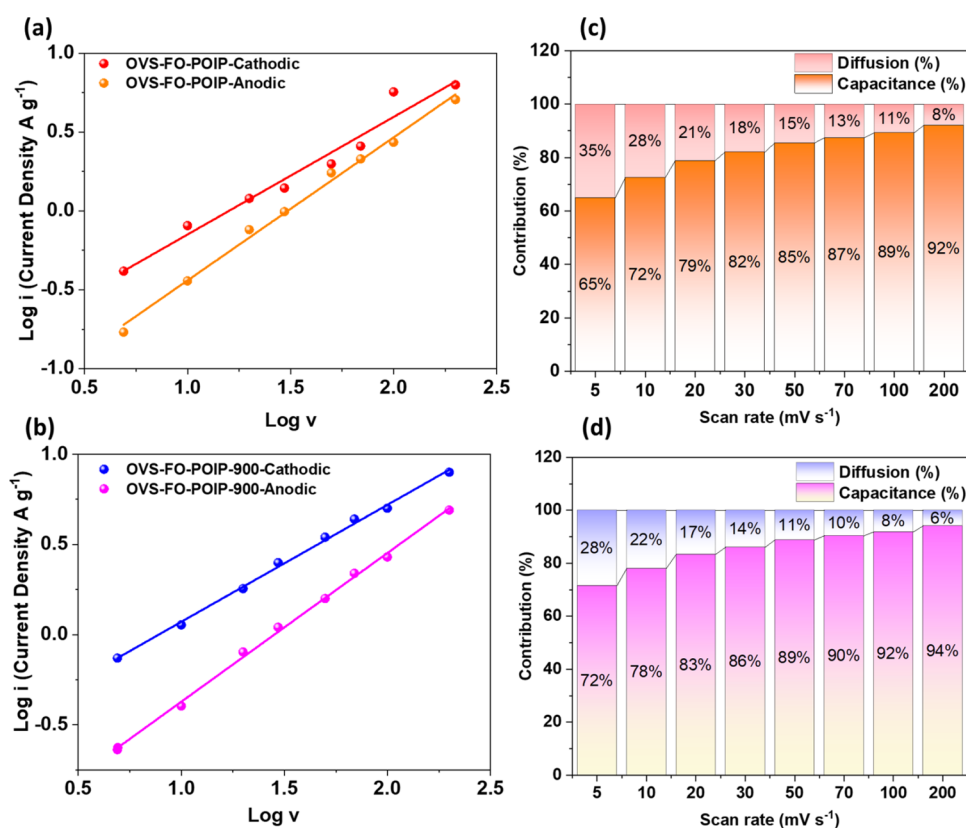
Figure 7. (a, b) Plots of log i against log ν of (a) OVS-FO-POIP and (b) OVS-FO-POIP-900. The relative contributions of the capacitive and diffusion-controlled charge storage of (c) OVS-FO-POIP and (d) OVS-FO-POIP-900 were recorded at different scan rates.

device. The resulting voltage—time curve during charge and discharge offers valuable insights into the supercapacitor's behavior. Figure 4c,4d presents the GCD curves of OVS-FO-POIP and OVS-FO-POIP-900, respectively, from 1 to 20 A g^{-1}. Specific capacitance is determined by the discharging time of the GCD curve, yielding values of 277 and 776 F g^{-1} for OVS-FO-POIP and OVS-FO-POIP-900, respectively, at 1 A g^{-1}. However, these values decrease with increasing current density, Figure 5a. When a supercapacitor is subjected to higher current rates during charge and discharge (galvanostatic conditions), the electrolyte's ions have less time to diffuse and arrive at the electrode surfaces. Consequently, there is incomplete utilization of the electrode surface area for charge storage, resulting in a reduction in effective capacitance observed at higher currents. Additionally, the resistance of both the electrode material and the electrolyte can become more significant at higher current rates. This increased resistance leads to voltage drops across the electrode—electrolyte interfaces, affecting the overall charge storage capacity and causing a decrease in specific capacitance. At 20 A g^{-1}, the particular capacitance falls to 150 F g^{-1} for OVS-FO-POIP and 500 F g^{-1} for OVS-FO-POIP-900. The precisely defined porosities and well-controlled pore size distribution of the crystalline phase of OVS-FO-POIP-900 provide ample space for ions to gather at the contact between the electrode and electrolyte, consequently enhancing the charge storage capacity. Moreover, the extensive surface area of OVS-FO-POIP-900 facilitates a greater number of electrochemical reactions, leading to increased capacitance. As depicted in Table S1, the active electrodes derived from OVS-FO-POIP and OVS-FO-POIP-900 materials demonstrated superior

electrochemical performance when compared to other electrode materials derived from POSS. We also assessed the capacitance retention (%) after 6000 cycles. Capacitance retention (%) is a crucial metric used to gauge the stability and long-term performance of capacitive energy storage devices like supercapacitors. It indicates the device's ability to maintain its initial capacitance over a specified number of charge—discharge cycles or extended operational periods. A high capacitance retention percentage signifies excellent stability and minimal degradation in capacitance over time or cycles, which is essential for ensuring reliability and durability, especially in applications requiring frequent cycling or prolonged usage. For OVS-FO-POIP and OVS-FO-POIP-900, the capacitance retention (%) is 96% and 98%, respectively, Figure 5b. Based on these electrochemical findings, these results underscore the remarkable performance of OVS-FO-POIP-900, indicating its potential as a material for supercapacitor applications.

Constructing a Symmetric Supercapacitor Coin Cell for the OVS-FO-POIP and OVS-FO-POIP-900. Furthermore, our investigation focused on the electrochemical performance of the polarized OVS-FO-POIP and the polarized OVS-FO-POIP-900 for a coin cell-based symmetric super-capacitor. Supercapacitors in the coin cell format typically employ electrode materials with high surface area and conductivity to maximize the charge storage capacity and efficiency. The separation membrane utilized in the symmetric device is Selemion's AMV (anionic membrane). CV profiles were acquired at scan speeds ranging from 5 to 200 mV s^{-1} within a positive potential region of 0−0.5 V. Figure 6a,6b illustrates the CV of the coin cell for OVS-FO-POIP and OVS-FO-POIP-900, respectively, displaying the rectangular shape
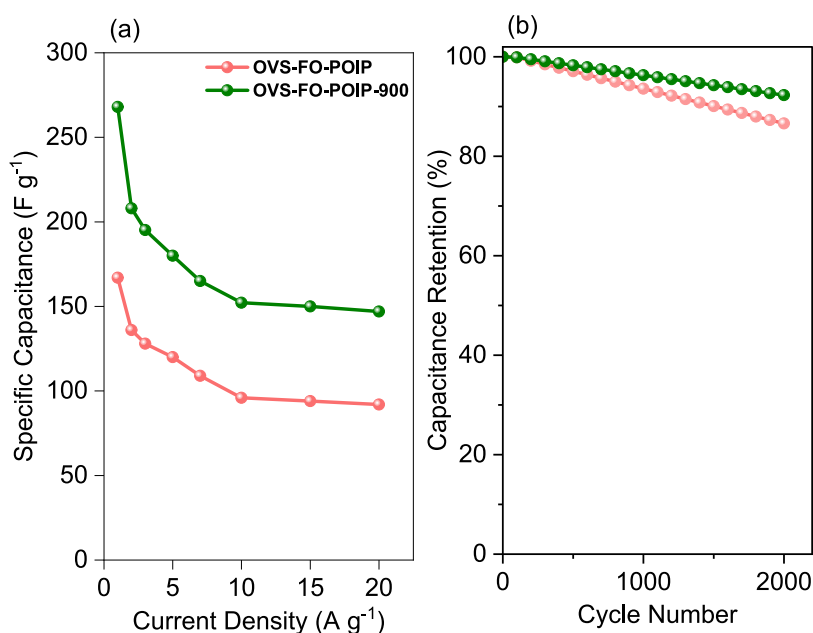
Figure 8. (a) Specific capacitance and (b) stability profile of the OVS-FO-POIP and the OVS-FO-POIP-900 symmetric coin cell.

characteristic of CV profiles and confirming the EDLC. The EDLC stores energy by physically separating charges at the electrode−electrolyte interface, rather than through traditional chemical reactions observed in batteries. This separation of charges forms an electric double layer, comprising ions from the electrolyte attracted to opposite charges on the electrode surface. The GCD tests for OVS-FO-POIP and OVS-FO-POIP-900, Figure 6c,d, revealed highly symmetric triangular shapes, demonstrating reversible ionic adsorption and desorption mechanisms and effective ion transport.[67,68]

The power law equation (eq 1) is utilized to assess the capacitive and diffusive contributions of OVS-FO-POIP and OVS-FO-POIP-900 in the symmetric device by graphing the correlation between the current and scan rate.[69]

$$i = av^b \qquad (1)$$

The constants "a" and "b" are involved, where "b" is determined by plotting $\log(i)$ against $\log(v)$. A slope value of 1 indicates a capacitive contribution. Figure 7a,7b displays $\log(i)$ plotted against log v for OVS-FO-POIP, yielding slopes of 0.6 and 0.71 for cathodic and anodic peaks, respectively. OVS-FO-POIP-900 exhibits slopes of 0.68 and 0.82 for cathodic and anodic peaks, respectively. The percentage contribution is computed using the following eq 2.[70]

$$i(V) = k1v + k2v^{1/2} \qquad (2)$$

Figure 7c,7d exhibits the percentage contributions of capacitance and diffusion depicted at various scan rates. In the symmetric device of the OVS-FO-POIP, 92% capacitive contribution is observed at 200 mV s^{-1}, decreasing to 65% at 5 mV s^{-1}. Conversely, OVS-FO-POIP-900 demonstrates 94% capacitive contribution, which diminishes to 72% at lower scan rates. These findings suggest the potential coexistence of capacitive and diffusion-controlled processes for energy storage in both samples within symmetric coin cells. Additionally, the higher capacitive contribution of OVS-FO-POIP-900 compared to OVS-FO-POIP is possibly attributed to its larger surface area, this material exhibits potential for use in energy storage applications. The specific capacitance obtained at 1 A

g^{-1} is 167 and 268 F g^{-1} for OVS-FO-POIP and OVS-FO-POIP-900, respectively. However, this capacitance decreases to 147 and 92 F g^{-1} for OVS-FO-POIP-900 and OVS-FO-POIP, respectively, with increasing current density up to 20 A g^{-1}, Figure 8a. Supercapacitors' stability, particularly in coin cell configurations, is paramount for ensuring reliable performance and long-term usage. GCD stability cycles entail controlled charge and discharge procedures at a constant current (under galvanostatic conditions) to evaluate the performance and stability of the supercapacitors. Stability is assessed in terms of capacitance retention (%) after 2000 GCD cycles. The capacitance retention (%) exhibited by OVS-FO-POIP-900 and OVS-FO-POIP is 92 and 86%, respectively Figure 8b.

The Ragone plot serves as a valuable tool for illustrating how various energy storage technologies, such as supercapacitors, balance power and energy densities. Remarkably, the OVS-FO-POIP-900 exhibits a notably high power density, peaking at 479 W/kg with an energy density of 9.33 Wh/kg. In contrast, the OVS-FO-POIP demonstrates a power density of 479 W/kg at an energy density of 3.73 Wh/kg, Figure 9. This characteristic makes them well-suited for applications prioritizing power delivery over total energy storage capacity, where frequent cycling and rapid response times are paramount.

To investigate the electrochemical properties of OVS-FO-POIP and OVS-FO-POIP-900, electrochemical impedance spectroscopy (EIS) was used, offering insights into their impedance, capacitance, and resistance (R_s and R_{ct}) across different frequencies. Nyquist plots for OVS-FO-POIP and OVS-FO-POIP-900 are depicted in Figure 10a before and after fitting and the equivalent-fitted circuit of OVS-FO-POIP-900 as presented in Figure 10b. Series resistances for OVS-FO-POIP and OVS-FO-POIP-900 were determined from the EIS data as 1.274 and 7.334 ohms, respectively, indicating similar electrochemical reactions across these electrode materials. However, notable differences were observed in their charge transfer resistances. OVS-FO-POIP-900 exhibited the lowest Rct among the electrodes at 10.24 ohms compared to OVS-FO-POIP, which registered 22 ohms, indicating enhanced conductivity. The frequency-dependent magnitude Bode plots
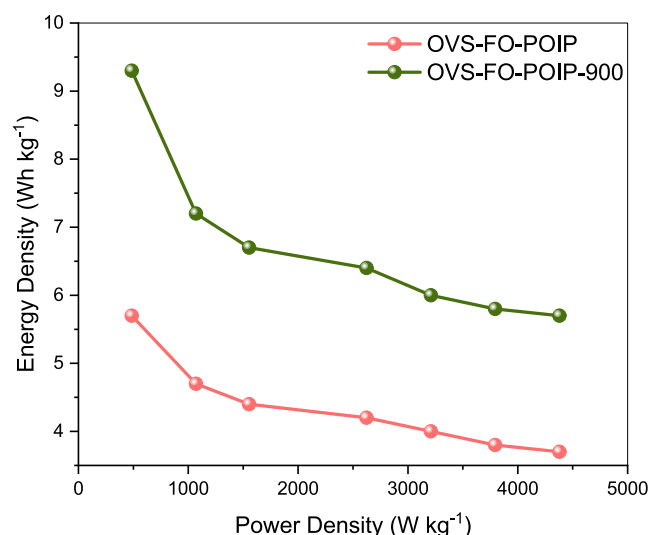
Figure 9. Ragone plot of the OVS-FO-POIP and OVS-FO-POIP-900 symmetric coin cell.

in Figure 10c showed substantial resistance at higher frequencies and negative slopes at lower frequencies, indicating that the capacitive behavior of OVS-FO-POIP and the capacitive behavior of OVS-FO-POIP-900 had extraordinary capacitive behavior. Additionally, the frequency-dependent phase-angle Bode graphs in Figure 10d illustrate the knee frequencies, representing the rate performance of the electrode materials. Notably, OVS-FO-POIP-900 exhibited the highest knee frequency, suggesting its potential as an electrode material for energy storage with enhanced rate performance.

CONCLUSIONS

We successfully synthesized the OVS-FO-POIP through the Heck reaction between the OVS and DBFO moieties and confirmed its structure via characteristic peaks observed in FTIR and solid-state ^{13}C NMR spectra. Subsequent carbonization and activation processes yielded porous OVS-FO-POIP-900 with a graphitic structure and a large surface area. For practical applications, electrochemical measurements further assessed the performance of both OVS-FO-POIP and OVS-FO-POIP-900 at 1 A g^{-1}; OVS-FO-POIP-900 demonstrated a specific capacitance of 776 F g^{-1}, while OVS-FO-POIP showed 271 F g^{-1}. Constructing symmetric devices allowed for additional evaluation, with OVS-FO-POIP-900 achieving a specific capacitance of 268 F g^{-1} compared to 167 F g^{-1} for OVS-FO-POIP in coin cell configurations. Both the OVS-FO-POIP and the OVS-FO-POIP-900 possess inherent porosity, facilitating efficient ion transport and diffusion
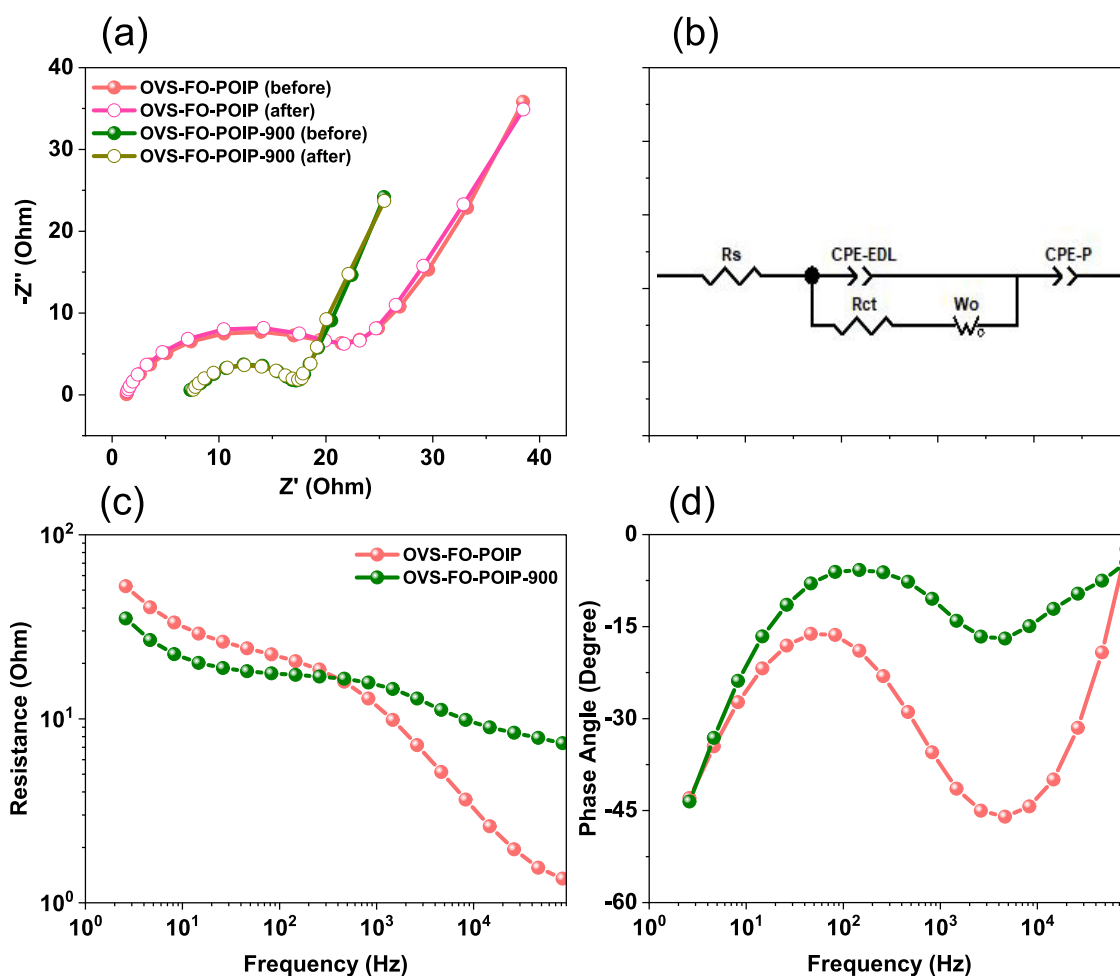
Figure 10. Electrochemical impedance spectrometry curves: (a) Nyquist plots (before and after) of the OVS-FO-POIP and OVS-FO-POIP-900 and (b) equivalent-fitted circuit of the OVS-FO-POIP-900, (c) Bode plot of frequency-dependent resistance (magnitude), and (d) Bode plot of frequency-dependent phase angles of the symmetric coin cell of the OVS-FO-OIP and the OVS-FO-POIP-900.

throughout the material, thereby enabling rapid charge/discharge processes and contributing to high capacitance. Overall, the electrochemical performance highlights that OVS-FO-POIP-900 is a superior substance for energy storage use.

ASSOCIATED CONTENT

Ⓢⓘ Supporting Information

The Supporting Information is available free of charge at https://pubs.acs.org/doi/10.1021/acsaem.4c01796.

> Characterizations; electrochemical analysis; measurements; ^{1}H NMR of DBFO; schematic synthesis of OVS-FO-POIP-900 from OVS-FO-POIP through carbonization and activation process; Raman spectrum of OVS-FO-POIP-900; specific capacitance of OVS-FO-POIP and OVS-FO-POIP-900 calculated from CV profiles; and performance comparison of supercapacitors using OVS-FO-POIP and OVS-FO-POIP-900 electrodes with previously described electrodes (PDF)

AUTHOR INFORMATION

Corresponding Authors

Mohamed Gamal Mohamed − *Department of Materials and Optoelectronic Science, College of Semiconductor and Advanced Technology Research, Center for Functional Polymers and Supramolecular Materials, National Sun Yat-Sen University, Kaohsiung 804, Taiwan; Department of Chemistry, Faculty of Science, Assiut University, Assiut 71516, Egypt;* ⓞ orcid.org/0000-0003-0301-8372; Email: mgamal.eldin12@yahoo.com

Shiao-Wei Kuo − *Department of Materials and Optoelectronic Science, College of Semiconductor and Advanced Technology Research, Center for Functional Polymers and Supramolecular Materials, National Sun Yat-Sen University, Kaohsiung 804, Taiwan; Department of Medicinal and Applied Chemistry, Kaohsiung Medical University, Kaohsiung 807, Taiwan;* ⓞ orcid.org/0000-0002-4306-7171; Email: kuosw@faculty.nsysu.edu.tw

Authors

Abdul Basit − *Department of Materials and Optoelectronic Science, College of Semiconductor and Advanced Technology Research, Center for Functional Polymers and Supramolecular Materials, National Sun Yat-Sen University, Kaohsiung 804, Taiwan*

Mohsin Ejaz − *Department of Materials and Optoelectronic Science, College of Semiconductor and Advanced Technology Research, Center for Functional Polymers and Supramolecular Materials, National Sun Yat-Sen University, Kaohsiung 804, Taiwan*

Bo Xuan Su − *Department of Materials and Optoelectronic Science, College of Semiconductor and Advanced Technology Research, Center for Functional Polymers and Supramolecular Materials, National Sun Yat-Sen University, Kaohsiung 804, Taiwan*

Hina Manzoor − *Department of Materials and Optoelectronic Science, College of Semiconductor and Advanced Technology Research, Center for Functional Polymers and Supramolecular Materials, National Sun Yat-Sen University, Kaohsiung 804, Taiwan*

Complete contact information is available at:
https://pubs.acs.org/10.1021/acsaem.4c01796

Notes

REFERENCES

(1) Samy, M. M.; Mohamed, M. G.; Sharma, S. U.; Chaganti, S. V.; Lee, J. T.; Kuo, S. W. An Ultrastable Tetrabenzonaphthalene-Linked conjugated microporous polymer functioning as a high-performance electrode for supercapacitors. *J. Taiwan Inst. Chem. Eng.* **2024**, *158*, No. 104750.

(2) Samy, M. M.; Mohamed, M. G.; Kuo, S. W. Pyrene-functionalized tetraphenylethylene polybenzoxazine for dispersing single-walled carbon nanotubes and energy storage. *Compos. Sci. Technol.* **2020**, *199*, No. 108360.

(3) Ejaz, M.; Mohamed, M. G.; Kuo, S. W. Solid state chemical transformation provides a fully benzoxazine-linked porous organic polymer displaying enhanced CO_2 capture and supercapacitor performance. *Polym. Chem.* **2023**, *14*, 2494−2509.

(4) Rafik, F.; Gualous, H.; Gallay, R.; Crausaz, A.; Berthon, A. Frequency, thermal and voltage supercapacitor characterization and modeling. *J. Power Sources* **2007**, *165*, 928−934.

(5) Mohamed, M. G.; Mansoure, T. H.; Takashi, Y.; Samy, M. M.; Chen, T.; Kuo, S. W. Ultrastable porous organic/inorganic polymers based on polyhedral oligomeric silsesquioxane (POSS) hybrids exhibiting high performance for thermal property and energy storage. *Microporous Mesoporous Mater.* **2021**, *328*, No. 111505.

(6) Chen, D.; Jiang, K.; Huang, T.; Shen, G. Recent advances in fiber supercapacitors: materials, device configurations, and applications. *Adv. Mater.* **2020**, *32*, No. 1901806.

(7) Wulan Septiani, N. L.; Kaneti, Y. V.; Fathoni, K. B.; Wang, J.; Ide, Y.; Yuliarto, B.; Dipojono, H. K.; Nanjundan, A. K.; Golberg, D.; Bando, Y.; et al. Self-assembly of nickel phosphate-based nanotubes into two-dimensional crumpled sheet-like architectures for high-performance asymmetric supercapacitors. *Nano. Energy* **2020**, *67*, No. 104270.

(8) Samy, M. M.; Mohamed, M. G.; El-Mahdy, A. F. M.; Mansoure, T. H.; Wu, K. C. W.; Kuo, S. W. High-performance supercapacitor electrodes prepared from dispersions of tetrabenzonaphthalene-based conjugated microporous polymers and carbon nanotubes. *ACS Appl. Mater. Interfaces* **2021**, *13*, 51906−51916.

(9) Mohamed, M. G.; Sharma, S. U.; Wang, P. T.; Ibrahim, M.; Lin, M. H.; Liu, C. L.; Ejaz, M.; Yen, H. J.; Kuo, S. W. Construction of fully π-conjugated, diyne-linked conjugated microporous polymers based on tetraphenylethene and dibenzo[g,p]chrysene units for energy storage. *Polym. Chem.* **2024**, *15*, 2827−2839.

(10) Mohamed, M. G.; Su, B. X.; Kuo, S. W. Robust Nitrogen-Doped Microporous Carbon via Crown Ether-Functionalized Benzoxazine-Linked Porous Organic Polymers for Enhanced CO_2 Adsorption and Supercapacitor Applications. *ACS Appl. Mater. Interfaces* **2024**, *16*, 40858−40872.

(11) Mohamed, M. G.; Ibrahim, M.; Chen, N. P.; Basit, A.; Kao, Y. C.; Mousa, A. Y.; Samy, M. M.; Kuo, S. W. Tetrabenzonaphthalene and Redox-Active Anthraquinone-Linked Conjugated Microporous Polymers as Organic Electrodes for Enhanced Energy Storage Efficiency. *ACS Appl. Energy Mater.* **2024**, *7*, 5582−5593.

(12) Du, X.; Wang, C.; Chen, M.; Jiao, Y.; Wang, J. Electrochemical performances of nanoparticle Fe_3O_4/activated carbon supercapacitor using KOH electrolyte solution. *J. Phys. Chem. C* **2009**, *113*, 2643−2646.

(13) Zhou, D.; Lin, H.; Zhang, F.; Niu, H.; Cui, L.; Wang, Q.; Qu, F. Freestanding MnO_2 nanoflakes/porous carbon nanofibers for high-

performance flexible supercapacitor electrodes. *Electrochim. Acta* **2015**, *161*, 427−435.

(14) Amin, K.; Ashraf, N.; Mao, L.; Faul, C. F.; Wei, Z. Conjugated microporous polymers for energy storage: Recent progress and challenges. *Nano Energy* **2021**, *85*, No. 105958.

(15) Samy, M. M.; Mohamed, M. G.; Kuo, S. W. Conjugated microporous polymers based on ferrocene units as highly efficient electrodes for energy storage. *Polymer* **2023**, *15*, 1095.

(16) Liu, S.; Kang, L.; Zhang, J.; Jung, E.; Lee, S.; Jun, S. C. Structural engineering and surface modification of MOF-derived cobalt-based hybrid nanosheets for flexible solid-state supercapacitors. *Energy Storage Mater.* **2020**, *32*, 167−177.

(17) Mohamed, M. G.; Chaganti, S. V.; Li, M.-S.; Samy, M. M.; Sharma, S. U.; Lee, J.-T.; Elsayed, M. H.; Chou, H.-H.; Kuo, S. W. Ultrastable porous organic polymers containing thianthrene and pyrene units as organic electrode materials for supercapacitors. *ACS Appl. Energy Mater.* **2022**, *S*, 6442−6452.

(18) Ejaz, M.; Mohamed, M. G.; Chen, Y. T.; Zhang, K.; Kuo, S. W. Porous carbon materials augmented with heteroatoms derived from hyperbranched biobased benzoxazine resins for enhanced CO_2 adsorption and exceptional supercapacitor performance. *J. Energy Storage* **2024**, *78*, No. 110166.

(19) Mohamed, M. G.; Sharma, S. U.; Yang, C. H.; Samy, M. M.; Mohammed, A. A.; Chaganti, S. V.; Lee, J. T.; Kuo, S. W. Anthraquinone-enriched conjugated microporous polymers as organic cathode materials for high-performance lithium-ion batteries. *ACS Appl. Energy Mater.* **2021**, *4*, 14628−14639.

(20) Zheng, S.; Miao, L.; Sun, T.; Li, L.; Ma, T.; Bao, J.; Tao, Z.; Chen, J. An extended carbonyl-rich conjugated polymer cathode for high-capacity lithium-ion batteries. *J. Mater. Chem. A* **2021**, *9*, 2700−2705.

(21) Kim, D.; Kang, J.; Yan, B.; Seong, K.-d.; Piao, Y. Piao. Ambient temperature synthesis of iron-doped porous nickel pyrophosphate nanoparticles with long-term chemical stability for high-performance oxygen evolution reaction catalysis and supercapacitors. *ACS Sustainable Chem. Eng.* **2020**, *8*, 2843−2853.

(22) Xu, C.; Li, Z.; Yang, C.; Zou, P.; Xie, B.; Lin, Z.; Zhang, Z.; Li, B.; Kang, F.; Wong, C.-P. An ultralong, highly oriented nickel-nanowire-array electrode scaffold for high-performance compressible pseudocapacitors. *Adv. Mater.* **2016**, *28*, 4105−4110.

(23) Assresahegn, B. D.; Bélanger, D. Multifunctional Carbon for Electrochemical Double-Layer Capacitors. *Adv. Funct. Mater.* **2015**, *25*, 6775−6785.

(24) Winter, M.; Brodd, R. J. What are batteries, fuel cells, and supercapacitors? *Chem. Rev.* **2004**, *104*, 4245−4270.

(25) Zhang, J.; Gu, M.; Chen, X. Supercapacitors for renewable energy applications: A review. *Micro Nano Energy* **2023**, *21*, No. 100229.

(26) Kaur, P.; Hupp, J. T.; Nguyen, S. T. Porous organic polymers in catalysis: opportunities and challenges. *ACS Catal.* **2011**, *1*, 819−835.

(27) Zhang, Y.; Riduan, S. N. Functional porous organic polymers for heterogeneous catalysis. *Chem. Soc. Rev.* **2012**, *41*, 2083−2094.

(28) Zou, X.; Ren, H.; Zhu, G. Topology-directed design of porous organic frameworks and their advanced applications. *Chem. Commun.* **2013**, *49*, 3925−3936.

(29) Zhang, T.; Xing, G.; Chen, W.; Chen, L. Porous organic polymers: a promising platform for efficient photocatalysis. *Mater. Chem. Front.* **2020**, *4*, 332−353.

(30) Day, G. S.; Drake, H. F.; Zhou, H.-C.; Ryder, M. R. Evolution of porous materials from ancient remedies to modern frameworks. *Commun. Chem.* **2021**, *4*, 114.

(31) Tan, L.; Tan, B. Hypercrosslinked porous polymer materials: design, synthesis, and applications. *Chem. Soc. Rev.* **2017**, *46*, 3322−3356.

(32) Wu, D.; Xu, F.; Sun, B.; Fu, R.; He, H.; Matyjaszewski, K. Design and preparation of porous polymers. *Chem. Rev.* **2012**, *112*, 3959−4015.

(33) McKeown, N. B.; Budd, P. M. Polymers of intrinsic microporosity (PIMs): organic materials for membrane separations, heterogeneous catalysis and hydrogen storage. *Chem. Soc. Rev.* **2006**, *35*, 675−683.

(34) Budd, P. M.; McKeown, N. B.; Fritsch, D. Free volume and intrinsic microporosity in polymers. *J. Mater. Chem.* **2005**, *15*, 1977−1986.

(35) Mohamed, M. G.; Elsayed, M. H.; Hassan, A. E.; Basit, A.; Mekhemer, I. M. A.; Chou, H. H.; Chen, K. H.; Kuo, S. W. Hybrid Porous Polymers Combination of Octavinylsilsesquioxane/Pyrene with Benzothiadiazole Units for Robust Energy Storage and Efficient Photocatalytic Hydrogen Production from Water. *ACS. Appl. Polym. Mater.* **2024**, *6*, 5945−5956.

(36) Mohamed, M. G.; Elsayed, M. H.; Ye, Y.; Samy, M. M.; Hassan, A. E.; Mansoure, T. H.; Wen, Z.; Chou, H. H.; Chen, K. H.; Kuo, S. W. Construction of Porous Organic/Inorganic Hybrid Polymers Based on Polyhedral Oligomeric Silsesquioxane for Energy Storage and Hydrogen Production from Water. *Polymers* **2023**, *15*, 182.

(37) Hsiao, C. W.; Elewa, A. M.; Mohamed, M. G.; Kuo, S. W. Highly stable hybrid porous polymers containing polyhedral oligomeric silsesquioxane (POSS)/Dibenzo[g,p]chrysene and Dibenzo[b,d]thiophene units for efficient Rhodamine B dye removal. *Sep. Purif. Technol.* **2024**, *332*, No. 125771.

(38) Mohamed, M. G.; Elsayed, M. H.; Li, C. J.; Hassan, A. E.; Mekhemer, I. M. A.; Musa, A. F.; Hussien, M. K.; Chen, L. C.; Chen, K. H.; Chou, H. H.; Kuo, S. W. Reticular design and alkyne bridge engineering in donor−π−acceptor type conjugated microporous polymers for boosting photocatalytic hydrogen evolution. *J. Mater. Chem. A* **2024**, *12*, 7693−7710.

(39) Chung, W. T.; Mekhemer, I. M. A.; Mohamed, M. G.; Elewa, A. M.; EL-Mahdy, A. F. M.; Chou, H. H.; Kuo, S. W.; Wu, K. C. W. Recent advances in metal/covalent organic frameworks based materials: Their synthesis, structure design and potential applications for hydrogen production. *Coord. Chem. Rev.* **2023**, *483*, No. 215066.

(40) Mousa, A. O.; Mohamed, M. G.; Chuang, C. H.; Kuo, S. W. Carbonized Aminal-Linked Porous Organic Polymers Containing Pyrene and Triazine Units for Gas Uptake and Energy Storage. *Polymers* **2023**, *15*, 1891.

(41) Mohamed, M. G.; Chang, W. C.; Chaganti, S. W.; Sharma, S. U.; Lee, J. T.; Kuo, S. W. Dispersion of ultrastable crown-ether-functionalized triphenylamine and pyrene-linked porous organic conjugated polymers with single-walled carbon nanotubes as high-performance electrodes for supercapacitors. *Polym. Chem.* **2023**, *14*, 4589−4601.

(42) Mousa, A. O.; Chuang, C. H.; Kuo, S. W.; Mohamed, M. G. Strategic Design and Synthesis of Ferrocene Linked Porous Organic Frameworks toward Tunable CO_2 Capture and Energy Storage. *Int. J. Mol. Sci.* **2023**, *24*, 12371.

(43) Mohamed, M. G.; Chang, S. Y.; Ejaz, M.; Samy, M. M.; Mousa, A. O.; Kuo, S. W. Design and Synthesis of Bisulfone-Linked Two-Dimensional Conjugated Microporous Polymers for CO_2 adsorption and Energy Storage. *Molecules* **2023**, *28*, 3234.

(44) Dawson, R.; Cooper, A. I.; Adams, D. J. Nanoporous organic polymer networks. *Prog. Polym. Sci.* **2012**, *37*, 530−563.

(45) Song, W.; Zhang, Y.; Tran, C. H.; Choi, H. K.; Yu, D.-G.; Kim, I. Porous organic polymers with defined morphologies: Synthesis, assembly, and emerging applications. *Prog. Polym. Sci.* **2023**, *142*, No. 101691.

(46) Chiang, C. H.; Mohamed, M. G.; Chen, W. C.; Madhu, M.; Tseng, W. L.; Kuo, S. W. Construction of Fluorescent Conjugated Polytriazole Containing Double-Decker Silsesquioxane: Click Polymerization and Thermal Stability. *Polymers* **2023**, *15*, 331.

(47) Kuo, S. W.; Chang, F. C. POSS related polymer nanocomposites. *Prog. Polym. Sci.* **2011**, *36*, 1649−1696.

(48) Kao, Y. C.; Lin, J. Y.; Chen, W. C.; Mohamed, M. G.; Huang, C. F.; Chen, J. H.; Kuo, S. W. High-Thermal Stable Epoxy Resin through Blending Nanoarchitectonics with Double-Decker-Shaped Polyhedral Silsesquioxane-Functionalized Benzoxazine Derivatives. *Polymers* **2024**, *16*, 112.

(49) Mohamed, M. G.; Kuo, S. W. Progress in the self-assembly of organic/inorganic polyhedral oligomeric silsesquioxane (POSS) hybrids. *Soft Matter* **2022**, *18*, 5535−5561.

(50) Mohamed, M. G.; Kuo, S. W. Functional silica and carbon nanocomposites based on polybenzoxazines. *Macromol. Chem. Phys.* **2019**, *220*, No. 1800306.

(51) Mohamed, M. G.; Kuo, S. W. Functional Polyimide/Polyhedral Oligomeric Silsesquioxane Nanocomposites. *Polymers* **2019**, *11*, 26.

(52) Li, Z.; Kong, J.; Wang, F.; He, C. Polyhedral oligomeric silsesquioxanes (POSSs): An important building block for organic optoelectronic materials. *J. Mater. Chem. C* **2017**, *5*, 5283−5298.

(53) Kausar, A. State-of-the-Art overview on polymer/POSS nanocomposite. *Polym.-Plast. Technol. Eng.* **2017**, *56*, 1401−1420.

(54) Chou, T. C.; Chen, W. C.; Mohamed, M. G.; Huang, Y. C.; Kuo, S. W. Organic-Inorganic Phenolic/POSS Hybrids Provide Highly Ordered Mesoporous Structures Templated by High Thermal Stability of PS-*b*-P4VP Diblock Copolymer. *Chem. - Eur. J.* **2023**, *29*, No. e202300538.

(55) Chen, F.; Lin, F.; Zhang, Q.; Cai, R.; Wu, Y.; Ma, X. Polyhedral oligomeric silsesquioxane hybrid polymers: well-defined architectural design and potential functional applications. *Macromol. Rapid Commun.* **2019**, *40*, No. 1900101.

(56) Shi, H.; Yang, J.; You, M.; Li, Z.; He, C. Polyhedral oligomeric silsesquioxanes (POSS)-based hybrid soft gels: Molecular design, material advantages, and emerging applications. *ACS Materials Lett.* **2020**, *2*, 296−316.

(57) Laine, R. M.; Roll, M. F. Polyhedral phenylsilsesquioxanes. *Macromolecules* **2011**, *44*, 1073−1109.

(58) Tanaka, K.; Chujo, Y. Advanced functional materials based on polyhedral oligomeric silsesquioxane (POSS). *J. Mater. Chem.* **2012**, *22*, 1733−1746.

(59) Marchesi, S.; Carniato, F.; Palinab, L.; Boccaleri, E. POSS as building-blocks for the preparation of polysilsesquioxanes through an innovative synthetic approach. *Dalton Trans.* **2015**, *44*, 2042−2046.

(60) Khan, S.; Iqbal, A. Organic polymers revolution: Applications and formation strategies, and future perspectives. *J. Polym. Sci. Eng.* **2023**, *6*, 3125.

(61) Li, Z.; Wu, D.; Liang, Y.; Fu, R.; Matyjaszewski, K. Synthesis of well-defined microporous carbons by molecular-scale templating with polyhedral oligomeric silsesquioxane moieties. *J. Am. Chem. Soc.* **2014**, *136*, 4805−4808.

(62) Liu, D.; Cheng, G.; Zhao, H.; Zeng, C.; Qu, D.; Xiao, L.; Tang, H.; Deng, Z.; Li, Y.; Su, B.-L. Self-assembly of polyhedral oligosilsesquioxane (POSS) into hierarchically ordered mesoporous carbons with uniform microporosity and nitrogen-doping for high performance supercapacitors. *Nano Energy* **2016**, *22*, 255−268.

(63) Yan, J.; Choi, J.-H.; Jeong, Y. G. Freestanding supercapacitor electrode applications of carbon nanofibers based on polyacrylonitrile and polyhedral oligomeric silsesquioxane. *Mater. Des.* **2018**, *139*, 72−80.

(64) Chen, Y. C.; Mohamed, M. G.; Chen, W. C.; Kuo, S. W. Construction of Ultrastable porous carbons materials derived from organic/inorganic double decker silsesquioxane (DDSQ) hybrid as a high-performance electrode for supercapacitor. *Mater. Today Chem.* **2023**, *34*, No. 101773.

(65) Soni, C. B.; Bera, S.; Sungjemmenla; Vineeth, S. K.; Kumar, H.; Kumar, V. Novel organic molecule enabling a highly-stable and reversible sodium metal anode for room-temperature sodium-metal batteries. *J. Energy Storage* **2023**, *71*, No. 108132.

(66) Ran, F. T.; Yang, X. B.; Xu, X. Q.; Li, S. W.; Liu, Y. Y.; Shao, L. Green activation of sustainable resources to synthesize nitrogen-doped oxygen-riched porous carbon nanosheets towards high-performance supercapacitor. *Chem. Eng. J.* **2021**, *412*, No. 128673.

(67) Wang, A.; Xu, W.; Sun, Y. J.; Sun, K.; Jiang, J. C. Heterogeneous activated carbon with graphitized shell and hydrophilic pores integrating high conductivity and pore affinity for excellent rate performance supercapacitors. *Fuel* **2022**, *310*, No. 122410.

(68) Ejaz, M.; Mohamed, M. G.; Sharma, S. U.; Lee, J. T.; Huang, C.-F.; Chen, T.; Kuo, S. W. An Ultrastable Porous Polyhedral Oligomeric Silsesquioxane/Tetraphenylthiophene Hybrid as a High-Performance Electrode for Supercapacitors. *Molecules* **2022**, *27*, 6238.

(69) Li, W. Y.; Wang, T.; Guo, J.; Liu, P. G.; Yin, X. W.; Wu, D. L. Organic resin based high surface area and N-enriched porous carbon nanosheets for supercapacitors. *Appl. Surf. Sci.* **2022**, *599*, No. 153885.

(70) Mousa, A. O.; Sharma, S. U.; Chaganti, S. V.; Mansoure, T. H.; Singh, P. N.; Ejaz, M.; Chuang, C. H.; Lee, J. T.; Kuo, S. W.; Mohamed, M. G. Designing Strategically Functionalized Conjugated Microporous Polymers with Pyrene and Perylenetetracarboxylic Dianhydride Moieties with Single-Walled Carbon Nanotubes to Enhance Supercapacitive Energy Storage Efficiency. *J. Power Sources* **2024**, *680*, No. 234624.